Non-exponential transverse relaxation decay in subcortical grey matter

Rita Oliveira[1*], Quentin Raynaud[1], Valerij Kiselev[2], Ileana Jelescu[3] , Antoine Lutti[1]

[1]Laboratory for Research in Neuroimaging, Department of Clinical Neuroscience, Lausanne University Hospital and University of Lausanne, Lausanne, Switzerland

[2]Medical Physics, Department of Radiology, Faculty of Medicine, University of Freiburg, Freiburg, Germany

[3]Department of Radiology, Lausanne University Hospital (CHUV) and University of Lausanne, Lausanne, Switzerland

*** Correspondence:**

Rita Oliveira: ana.veiga-de-oliveira@chuv.ch

Keywords: transverse relaxation, $\boldsymbol{R_2^*}$, iron, basal ganglia, non-exponential

Abstract

Inclusions of magnetic materials within brain tissue affect the decay of the MRI signal due to transverse relaxation. Theoretical studies of the gradient-echo signal anticipate a transition of the signal decay from Gaussian at short echo times to exponential at long echo times. However, transverse relaxation signal decay is widely reported to follow a simple exponential behaviour, with a rate R_2^*. Here, we provide experimental evidence of non-exponential signal decay due to transverse relaxation in human subcortical grey matter, from gradient-echo MRI data acquired *in vivo* at 3T.

The signal decay follows the qualitative behaviour predicted by theoretical models of the effect of magnetic inclusions on the MRI signal. In subcortical grey matter, such models lead to an improved fit to experimental data than the traditionally used exponential model. Amongst subcortical regions, the strongest deviations from exponential behaviour take place in the substantia nigra and globus pallidus.

From the estimates of the signal model parameters, we assess the properties of the magnetic inclusions at the source of the effect within brain tissue. In the limiting case of the static dephasing regime, the magnetic susceptibility and volume fractions of the inclusions range from 1.2 to 2.6 ppm SI units and from 0.03 to 0.06 between subcortical regions, respectively. The higher estimates in the substantia nigra and globus pallidus are consistent with *ex vivo* histological studies and suggest a dominant contribution of iron-rich inclusions. In the limiting case of the diffusion narrowing regime, the typical size of the magnetic inclusions is ~3 μm, representative of typical iron-containing cells.

Non-exponential transverse relaxation signal decay in subcortical grey matter provides new means to characterize the spatial distribution of magnetic inclusions within brain tissue with increased specificity.

1 Introduction

In Magnetic Resonance Imaging (MRI) data, the decay of the gradient-echo signal due to transverse relaxation is widely considered to follow an exponential behaviour with a rate R_2^* (Weiskopf et al., 2014). Estimates of R_2^* correlate with iron concentration within brain tissue (Péran et al., 2009; Yao et al., 2009; Fukunaga et al., 2010; Langkammer et al., 2010), a property of primary importance for the study of the brain. Iron indeed plays a crucial role in various biological processes such as myelin synthesis, energy production, and neurotransmitter synthesis and signalling (Hare et al., 2013; Möller et al., 2019). Abnormal accumulation of iron also constitutes a hallmark of neurodegenerative disorders such as Parkinson's Disease (Gerlach et al., 1994; Thompson et al., 2001; Ward et al., 2014). As a result, R_2^* mapping data are used extensively for the monitoring of iron-related brain changes, in particular, in neurodegenerative diseases (Ulla et al., 2013; Damulina et al., 2020).

Inclusions of magnetic material within brain tissue such as iron-loaded cells, myelin, or blood vessels, induce microscopic inhomogeneities of the magnetic field which can result in a non-exponential signal decay (Haacke et al., 2005; Kiselev and Novikov, 2018). According to theoretical studies, such decay displays a Gaussian behaviour at short echo times followed by an exponential behaviour at longer echo times (Yablonskiy and Haacke, 1994; Jensen and Chandra, 2000a; Kiselev and Novikov, 2002, 2018; Sukstanskii and Yablonskiy, 2003). While this behaviour has been reported in suspensions of paramagnetic beads (Storey et al., 2015), in *ex vivo* brain samples (Jensen and Chandra, 2000a) and *in vivo* blood vessels (Ulrich and Yablonskiy, 2016), no evidence has been presented from iron-rich subcortical grey matter regions *in vivo*.

The mechanisms that underlie transverse relaxation in the presence of magnetic inclusions can be described under two limiting regimes (see Novikov et al., 2018 for a review). In the static dephasing regime (SDR), water diffusion can be neglected and signal decay arises from the spatial inhomogeneities of the magnetic field generated by the inclusions (Yablonskiy and Haacke, 1994; Jensen and Chandra, 2000b). In the diffusion narrowing regime (DNR) (Anderson and Weiss, 1953; Kennan et al., 1994; Jensen and Chandra, 2000a; Kiselev and Novikov, 2002; Sukstanskii and Yablonskiy, 2003), signal decay arises primarily from the diffusion of water molecules across these spatial inhomogeneities. The large differences in the relaxation rate measured from spin-echo and gradient-echo data come in support of the SDR as a plausible mechanism for transverse relaxation in subcortical grey matter regions (Sedlacik et al., 2014; Brammerloh et al., 2021). On the other hand, investigations of the relationship between R_2^* and MRI measures of magnetic susceptibility in the basal ganglia have suggested the DNR as the most plausible regime (Yablonskiy et al., 2021).

In this work, we provide experimental evidence of non-exponential MRI signal decay due to transverse relaxation in subcortical brain regions, in gradient-echo data acquired *in vivo* at 3T. We fitted the signal decay with an interpolating expression and theoretical models of the effect of magnetic inclusions within brain tissue on the MRI signal (Anderson and Weiss, 1953; Jensen and Chandra, 2000a; Sukstanskii and Yablonskiy, 2003). From the model parameter estimates of the Gaussian and exponential parts of the signal decay, we assessed the properties of the magnetic inclusions within the tissue at the source of the transverse relaxation. We discuss the plausibility of the magnetic inclusion property estimates in view of the existing *ex vivo* literature.

2 Theory

2.1 Transverse relaxation in the presence of magnetic material

Existing biophysical models of the effect of non-heme iron on transverse relaxation all rely on essentially the same model of randomly distributed magnetized inclusions, typically of spherical form. Differences between existing models involve the dominating dephasing regime and secondary assumptions. In particular, models derived in the DNR differ in the form of the auto-correlation function of the Larmor frequency experienced by diffusing spins. In the model of Anderson and Weiss, 1953 (AW), this auto-correlation function is assumed to take an exponential form. In the model of Sukstanskii and Yablonskiy, 2003 and Jensen and Chandra, 2000 (SY) the auto-correlation function was derived analytically from spin diffusion within brain tissue. All existing models predict asymptotic behaviours of the signal decay of the following forms:

$$\mathrm{S} \approx S_0 \exp\left(-\frac{1}{2}\,\langle\Omega^2\rangle {T_E}^2 - R_{2,nano}T_E\right), \quad T_E \ll \frac{R^*_{2,micro}}{\langle\Omega^2\rangle} \tag{1}$$

$$\mathrm{S} \approx S_0 \exp\left(-R^*_{2,micro}T_E - R_{2,nano}T_E\right), \quad T_E \gg \frac{R^*_{2,micro}}{\langle\Omega^2\rangle} \tag{2}$$

where S_0 is the signal amplitude at $T_E = 0$, $R_{2,nano}$ is the transverse relaxation rate due to spin-spin interactions at the molecular/nanoscopic scale, $\langle\Omega^2\rangle$ is the variance of the field inhomogeneities induced by the magnetic inclusions (Novikov et al., 2018) and $R^*_{2,micro}$ is the transverse relaxation rate at long echo times. Parametric evaluation of these expressions was conducted with the Padé approximation, which is a flexible model-free signal representation (Novikov et al., 2018), derived from a fraction of two polynomials with coefficients adjusted to satisfy the required asymptotic forms at the short- and long-time limits:

$$\mathrm{S}_{Padé} = S_0 \exp\left(-\frac{\langle\Omega^2\rangle {T_E}^2}{2\left(1 + \frac{\langle\Omega^2\rangle}{2R^*_{2,micro}}T_E\right)} - R_{2,nano}T_E\right) \tag{3}$$

We also used the AW and SY models after parameterization in terms of $\langle\Omega^2\rangle$ and $R^*_{2,micro}$:

$$\mathrm{S}_{AW} = S_0 \exp\left(-\frac{{R^*_{2,micro}}^2}{\langle\Omega^2\rangle}\left(\frac{\langle\Omega^2\rangle}{R^*_{2,micro}}T_E + e^{-\frac{\langle\Omega^2\rangle}{R^*_{2,micro}}T_E} - 1\right) - R_{2,nano}T_E\right) \tag{4}$$

$$\mathrm{S}_{SY} = S_0 \exp\left(-\frac{{R^*_{2,micro}}^2}{\langle\Omega^2\rangle}\left(\frac{\langle\Omega^2\rangle}{R^*_{2,micro}}T_E - \sqrt{1 + 2\frac{\langle\Omega^2\rangle}{R^*_{2,micro}}T_E} + 1\right) - R_{2,nano}T_E\right) \tag{5}$$

The exponential approximation of the signal is simply:

$$\mathrm{S}_{Exp} = S_0 \cdot \exp(-R^*_2 T_E) \tag{6}$$

with $R^*_2 = R^*_{2,micro} + R_{2,nano}$.

2.2 Microscopic underpinnings of non-exponential decay

In a second step, we link the detected parameters $R^*_{2,micro}$ and $\langle\Omega^2\rangle$ to the microstructural properties of the magnetic material within brain tissue assuming it is accumulated in spherical inclusions. The mean square frequency deviation $\langle\Omega^2\rangle$ of the magnetic field inhomogeneities generated by randomly distributed spherical inclusions is (Yablonskiy and Haacke, 1994; Jensen and Chandra, 2000a; Sukstanskii and Yablonskiy, 2003):

$$\langle\Omega^2\rangle = \frac{4}{45}\zeta \cdot (1-\zeta)(\gamma B_0 \Delta\chi)^2 \approx \frac{4}{45}\zeta \cdot (\gamma B_0 \Delta\chi)^2 \tag{7}$$

where $\zeta \ll 1$ is the volume fraction of the magnetic inclusions, $\Delta\chi$ is their susceptibility difference with the surrounding tissue (SI units), γ the gyromagnetic ratio ($2.675 \cdot 10^8\ rad\ s^{-1}T^{-1}$) and B_0 the main magnetic field. Note that $\langle\Omega^2\rangle$ is the field variance within a voxel, which differs from the frequency variance at the surface of a single sphere: $\langle {\Omega_s}^2\rangle = \frac{4}{45}\,(\gamma B_0\,\Delta\chi)^2$.

In the framework of the SDR (Yablonskiy and Haacke, 1994) and DNR (Jensen and Chandra, 2000a; Sukstanskii and Yablonskiy, 2003) the relaxation rate is described by the following equations:

$$R^*_{2,micro} = \lambda_{SDR}\zeta\gamma B_0\Delta\chi, \qquad \lambda_{SDR} \approx 0.4031 \tag{8a}$$

$$R^*_{2,micro} = \lambda_{DNR}\zeta\gamma^2 B_0^2\Delta\chi^2\tau, \quad \lambda_{DNR} = \frac{16}{75} \tag{8b}$$

where $\tau = \frac{r^2}{6D}$ is the time scale for water molecules to diffuse away from a spherical magnetic inclusion of radius r. D is the water diffusion coefficient in tissue (1 μm^2/ms).

In the DNR, the dimensionless parameter $\alpha = \tau\sqrt{\langle\Omega^2\rangle}$ (Storey et al., 2015; Kiselev and Novikov, 2018) represents the amount of spin dephasing induced by the field inhomogeneities over the period τ. The value of α regulates the dephasing regime with $\alpha \ll 1$ characterizing the DNR and $\alpha \gg 1$ the SDR.

3 Methods

3.1 Participant cohort

MRI data were acquired from 5 healthy volunteers (2 females, mean age=32±9 years old). The study received approval by the local ethics committee and all volunteers gave written informed consent for their participation.

3.2 Data acquisition

MRI data were acquired on a 3T whole-body MRI system (Magnetom Prisma; Siemens Medical Systems, Erlangen, Germany) with a 64-channel receive head coil. The MRI protocol consisted of multi-echo 3D fast low-angle shot (FLASH) acquisitions with a bipolar readout. Image resolution was 1.2 mm^3 isotropic, with a field of view 208×192×144 mm along the read and two phase-encode directions. 16 gradient-echo images were acquired with an echo time T_E ranging from 1.25 to 19.25 ms, with 1.2 ms inter-echo spacing (repetition time T_R = 23.2 ms). Partial Fourier (factor 6/8) was used in the phase and partition directions. Three repetitions were conducted on each participant and the total nominal acquisition time was 18min09s.

An optical tracking prospective motion correction system (KinetiCor, HI, Honolulu) was used to reduce image degradation due to head motion (Zaitsev et al., 2006; Maclaren et al., 2012). The cardiac pulsation of the participants was recorded using a finger pulse oximeter. To minimize the effect of cardiac-induced noise on the images, data acquisition was suspended during the systolic period of the cardiac cycle, taken to last for a duration of 300 ms (Raynaud et al., 2023). For a heart rate of 80 beats per minute, this resulted in an increase in scan time by approximately 40%. The quality index of the data laid within a narrow range across participants and did not exceed 3.7 s^{-1} (Fig. S1), indicative of high-quality data (Castella et al., 2018; Lutti et al., 2022; Corbin et al., 2023).

For the computation of MTsat maps (Helms et al., 2008b), multi-echo 3D FLASH images were acquired with magnetization transfer-, proton density- and T1-weighted contrasts (radio-frequency excitation flip angle = 6º, 6º and 21º, respectively; repetition time TR=24.5 ms). 8 echo images were acquired for the T1- and proton density-weighted contrasts and 6 for the magnetization transfer-weighted contrast. Image resolution was 1 mm^3 isotropic, and the image field of view was 176×240×256 mm. B1-field mapping data was acquired (4 mm^3 voxel size, TR/TE = 500/39.1 ms) to correct RF transmit field inhomogeneity effects on the MTsat maps (Lutti et al., 2010, 2012). For correction of image distortions in the B1 map data, B0-field map data was acquired with a 2D double-echo FLASH, TR=1020 ms, α =90◦, TE1/TE2 = 10/12.46 ms, BW = 260 Hz/pixel, slice thickness = 2 mm.

3.3 Anatomical imaging processing

MTsat maps were calculated from the magnetization transfer-, proton density- and T1-weighted images with the hMRI toolbox (Tabelow et al., 2019), as described in Helms et al., 2008b, 2008a. MTsat maps were segmented into grey and white matter tissue probability maps using the Statistical Parametric Mapping software (SPM12, Wellcome Centre for Human Neuroimaging, London) (Ashburner and Friston, 2005). A grey matter mask was computed by selecting voxels with a grey matter probability above 0.95. As B0-field inhomogeneities affect transverse relaxation, regions with inhomogeneous field (e.g. orbitofrontal cortex, inferior temporal lobe, amygdala) were removed from the grey matter mask. Globus pallidus (GP), putamen, thalamus, and caudate regions of interest (ROI) were defined from the grey matter mask and the regional labels of the Neuromorphometrics atlas (http:// neuromorphometrics.com/). As no label exists for the substantia nigra (SN), this region was delineated using an *ad hoc* procedure, from a cuboid placed appropriately in the space of each MTsat map. Within this cuboid, SN voxels were identified from the grey matter voxels labelled as brainstem and ventral diencephalon in the Neuromorphometrics atlas.

3.4 Fitting of the transverse relaxation decay

Data were analyzed using bespoke analysis scripts written with MATLAB R2021a (The Mathworks, Natick, MA). The gradient-echo data were denoised using the Marchenko Pastur-PCA method described in (Does et al., 2019). The PCA decomposition of the signal decay was conducted from the raw signals within the grey matter mask in cubic regions of 8x8x8 voxels. At each voxel, we removed scaling and additive effects between the signal decays acquired across repetitions, due to e.g. head motion in the spatially varying sensitivity profile of the receive coil. To suppress the noise floor in the magnitude images, background voxels outside the head were identified from the segmentation of the first gradient-echo image using SPM12 segmentation (Ashburner and Friston, 2005). The distribution of signal intensities across noise voxels was fitted assuming a Rician distribution and the resulting value of the noncentrality parameter was deducted from the signal intensities.

Fitting of the transverse relaxation decay with the analytical expressions of Section 2.1 involved the multi-echo data acquired across all repetitions simultaneously and was conducted using a dictionary-based approach. The columns of the dictionary contained signal decays predicted by all combinations of model parameter values. For all expressions, the $R^*_{2,micro}$ ranged from $1x10^{-3}$ to $80x10^{-3}$ ms^{-1}. The $\langle\Omega^2\rangle$ parameter ranged from $1x10^{-4}$ to $4x10^{-2}$ ms^{-2} for the Padé and AW models and from $1x10^{-4}$ to $8x10^{-2}$ ms^{-2} for the SY model. $R_{2,nano}$ was set to 10 s^{-1} (Jensen and Chandra, 2000a; Sedlacik et al., 2014; Brammerloh et al., 2021). To facilitate the visualization of the signal decays, both the data and dictionary columns were low-pass filtered prior to fitting, with a Butterworth filter of order 5 and a cut-off frequency

of 0.2 of the Nyquist rate. At each voxel, fitting the multi-echo data involved estimating the value of S_0 for each column of the dictionary. The solution was the set of parameter values of the dictionary column where the fitting residual was minimum.

While the Padé expression lacks a theoretical basis, we refer henceforward to all three analytical expressions (Eq. 3-5) as models of the MRI signal for the sake of simplicity. The goodness of fit of each model was estimated from the mean squared error of the fit (MSE) and the Akaike Information Criterion (AIC), which includes a penalty for model complexity. Lower MSE and AIC values indicate a better model fit. Model parameter estimates for the five regions of interest were extracted from all voxels and all subjects after the removal of the voxels where MSE>10, indicative of spurious effects in the data such as physiological noise. We also excluded voxels where the transition from Gaussian to exponential behaviour took place over a timescale $\frac{R^*_{2,micro}}{\langle \Omega^2 \rangle} < 0.5$ ms, too short to be robustly detectable.

3.5 Microscopic underpinnings of non-exponential decay

From the estimates of $R^*_{2,micro}$ and $\langle \Omega^2 \rangle$ et each voxel, we estimated the properties of the magnetic inclusions within brain tissue at the source of the non-exponential decay. Under the assumption of the SDR, we estimated the magnetic susceptibility ($\Delta\chi$) and volume fractions (ζ) of the inclusions (Eqs. 7 and 8a). The product of these quantities provides estimates of the MRI magnetic susceptibility obtained using Quantitative Susceptibility Mapping (QSM) (Li and Leigh, 2004; Schweser et al., 2011; Deistung et al., 2017), which can be calculated directly from the values of $R^*_{2,micro}$:

$$\chi_{MRI} = \zeta \Delta\chi = \frac{R^*_{2,micro}}{0.4031 \gamma B_0} \tag{9}$$

Under the assumption of the DNR, the model parameters $R^*_{2,micro}$ and $\langle \Omega^2 \rangle$ depend on three properties of the magnetic inclusions ($\Delta\chi$, ζ, and τ), which cannot be estimated from $R^*_{2,micro}$ and $\langle \Omega^2 \rangle$ alone. We estimated $\alpha = \tau\sqrt{\langle \Omega^2 \rangle}$ and τ instead (Eqs. 7 and 8b).

We conducted non-parametric Kruskal-Wallis statistical tests of inter-regional differences in the estimates of $\Delta\chi$ and ζ obtained under the assumption of the SDR (*kruskalwallis* function in Matlab 2021). Post-hoc Tukey's HSD tests were conducted subsequently to identify the pairs of regions at the source of these differences (*multcompare* function in Matlab). The effect size was computed using the cliff's delta to quantify the magnitude of differences between regions.

4 Results

4.1 Non-exponential transverse decay in basal ganglia and thalamus

At short echo times (T_E <5-10ms), transverse signal decay in the basal ganglia and thalamus (Fig. 1) displays systematic deviations from exponential behaviour (green line in Fig. 1): the logarithm of the signal exhibits an initial quadratic form, with a transition towards a linear dependence at longer times. This behaviour is consistent with the effect of magnetic inclusions on the MRI signal predicted by theoretical studies (see Kiselev and Novikov, 2018 for a review).

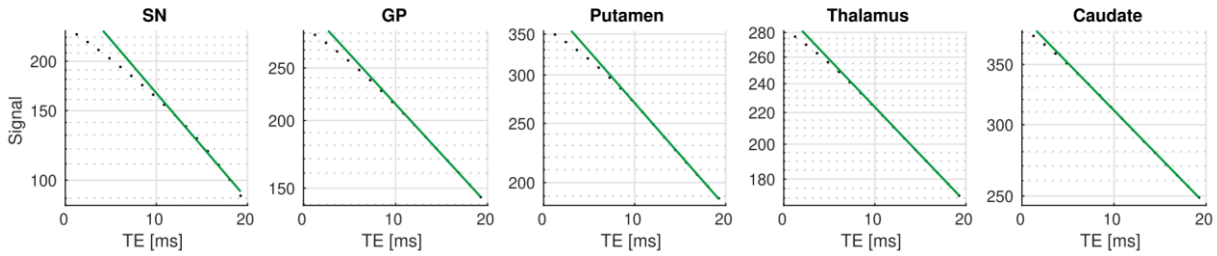

Fig. 1. Example transverse relaxation decays in the basal ganglia and thalamus (semilog-scale). The green line shows the exponential decay fit at long echo times (T_E>10ms). At short echo times (TE≲5ms), the data displays a quadratic decay consistent with the effect of magnetic inclusions on the MRI signal predicted by theoretical studies (Yablonskiy and Haacke, 1994; Jensen and Chandra, 2000a; Sukstanskii and Yablonskiy, 2003).

The non-exponential models of transverse relaxation (Padé, AW, SY) can account for the non-exponential decay of the MRI signal at short times, leading to an improved fit of the data (Fig. 2A). The residual levels are largely consistent across the non-exponential models (MSE ~1.3), a factor of ~3-4 smaller than for the exponential fit (Fig. 2B). The differences in the values of the AIC (~60, Fig. 2C) show that this residual decrease goes beyond that expected from the higher number of parameters with non-exponential models.

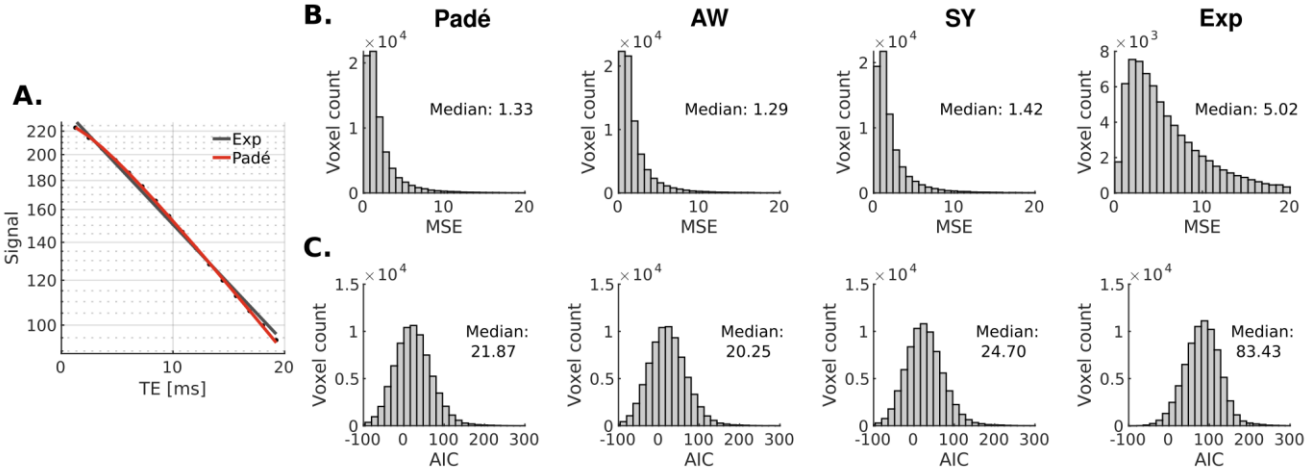

Fig. 2. Residual levels across signal models. Non-exponential models of transverse relaxation (*e.g.* Padé) can account for the non-exponential decay at short times, leading to an improved fit of the data (A). As a result, the residual levels (MSE) are reduced by ~3-4 across subcortical regions, consistently for all non-exponential models (B). This residual decrease leads to a decrease of the AIC by ~60, beyond that expected from the higher number of parameters of non-exponential models (C).

The ratio of the MSE from the exponential fit over those from the non-exponential fits is higher in subcortical regions (average ~6) than in cortical grey matter (average ~3, Fig. 3). This shows that non-exponential signal decays take place primarily in the subcortical regions.

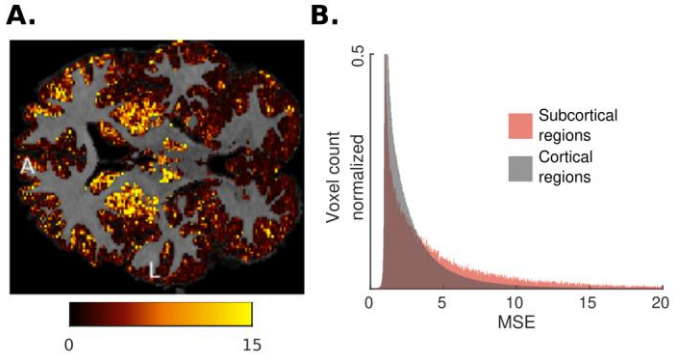

Fig. 3. Example spatial distribution of the ratio of the MSE from the exponential fit over the Padé signal model fit (A). The higher ratio values in subcortical regions (average ~6) indicate that the strongest deviations from exponential behaviour take place in these areas (B). L – left; A – anterior.

4.2 Estimates of the MRI signal model parameters

Non-exponential signal decays were reliably detected with $\frac{R^*_{2,micro}}{\langle\Omega^2\rangle} > 0.5$ ms in 86/85/86/88/85% of voxels in the SN/GP/putamen/thalamus/caudate, respectively. In these voxels, the non-exponential models (Padé, AW, SY) lead to estimates of $R^*_{2,micro}$ that are respectively 37%, 30%, and 54% higher than the exponential approximation (Fig. 4A).

The estimates of $R^*_{2,micro}$ and $\langle\Omega^2\rangle$ are spatially organised and are consistent between anatomical regions (Fig. 4). The values of $R^*_{2,micro}$ and $\langle\Omega^2\rangle$ are higher in the GP and the SN, consistent with histological measures of iron concentration in brain tissue (Hallgren and Sourander, 1958) and with the expected dependence of these parameters on iron content (Eqs. 7 and 8).

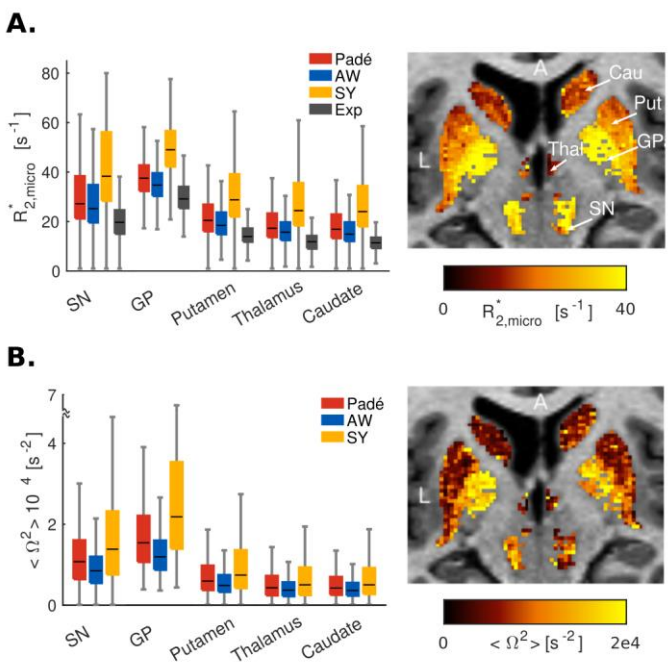

Fig. 4. Non-exponential model parameter estimates. Estimates of $R^*_{2,micro}$ (A) and $\langle\Omega^2\rangle$ (B) are highest in the GP followed by the SN, in agreement with histological measures of iron concentration (Hallgren and Sourander, 1958) and Eqs. 7 and 8. The example maps of $R^*_{2,micro}$ and $\langle\Omega^2\rangle$ were obtained from the AW model. L – left; A – anterior; Cau – caudate; Put – putamen; GP – globus pallidus; Thal – thalamus; SN – substantia nigra.

The SY model yields systematically higher values of $R^*_{2,micro}$ and $\langle\Omega^2\rangle$ than the AW and Padé approximation (~30-50%). This arises from the square-root term in the SY signal equation (Eq. 5), which brings a slow modulation of the signal over the range of echo times. As a result, the decay rate at very large echo times predicted by the SY model ($R_2(\infty)$) shows a steeper slope than the one observable experimentally (Fig. 5). On the other hand, the AW model converges to an exponential decay faster and the predicted decay rate at long echo times matches the slope of the data. Results from the Padé approximation and the AW model are largely consistent.

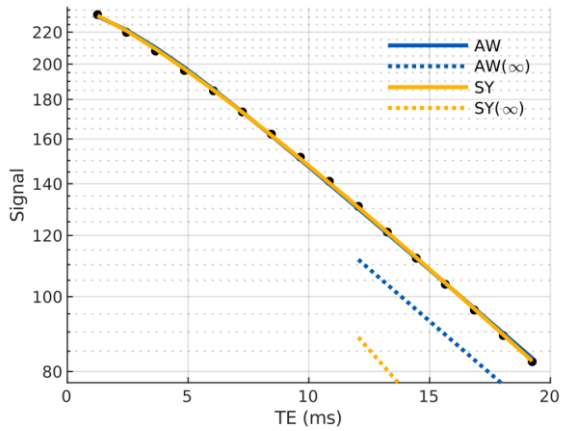

Fig. 5. Example transverse relaxation decay and fit with the AW (solid blue line) and SY (solid yellow line) models. Semi-log scale. The dashed lines correspond to the asymptotic behaviour of each model in the long-time limit $R_2(\infty)$. The slow convergence of the SY model towards an exponential decay leads to systematic differences between $R_2(\infty)$ and the decay rate observable experimentally.

4.3 Characterization of magnetic inclusions within subcortical tissue

From the estimates of the MRI signal parameters $R^*_{2,micro}$ and $\langle\Omega^2\rangle$, we characterized the properties of the magnetic inclusions present within brain tissue, at the source of the non-exponential decay. Under the assumption of the SDR, the estimates of $R^*_{2,micro}$ and $\langle\Omega^2\rangle$ were used to estimate the volume fraction (ζ) and magnetic susceptibility ($\Delta\chi$) of the inclusions (Eqs. 7 and 8a). Iron-rich regions such as the GP and SN display larger values of ζ (median value: 0.056 and 0.044 from the AW signal model respectively, Fig. 6) followed by the putamen (0.038) and caudate and thalamus (0.033). The SY model yields higher estimates of ζ due to the systematic differences in the $R^*_{2,micro}$ and $\langle\Omega^2\rangle$ estimates highlighted above. The median of the estimates of the magnetic susceptibility of the inclusions ($\Delta\chi$) ranges from 1.2 to 2.6 ppm. They are larger in the GP and SN (median $\Delta\chi$~2.0 ppm and 1.8 ppm respectively from the AW signal model), followed by the putamen ($\Delta\chi$~1.6 ppm) and caudate and thalamus ($\Delta\chi$~1.4 ppm). Assuming that ferritin is the only source of magnetic material within the inclusions, these estimates of $\Delta\chi$ indicate iron concentrations C_{Fe} of ~1.4, 1.5, 1.2, 1.1, and 1.1 mg/g in the SN, GP, putamen, thalamus and caudate, respectively, following $\Delta\chi = \chi_{eff}\rho C_{Fe}$ with the effective mass susceptibility of ferritin-bound iron χ_{eff}~1.3 ppm m^3/g (Schenck, 1992) calculated at a temperature of 310K and assuming a brain tissue density ρ~1.05 g/cm^3 (Barber et al., 1970).

The Kruskal-Wallis tests revealed statistically significant differences in $\Delta\chi$ between at least two ROIs (F(4, 69373) = [1155], p < 0.001 for the AW model). The corresponding Tukey's HSD test for multiple comparisons found significant differences between $\Delta\chi$ estimates from all ROIs (p<0.001) with small effect sizes, except between the thalamus and caudate where

no significance was found. The SN and GP showed the strongest effect sizes (>0.14) compared to the remaining regions.

Similarly, the Kruskal-Wallis tests revealed statistically significant differences in ζ between at least two ROIs (F(4, 69373) = [612], p < 0.001 for the AW model). The corresponding Tukey's HSD test showed significant differences between the ζ estimates from the GP and those from the putamen, thalamus, and caudate with the largest effect size (>0.30). Other inter-regional differences (except those between the thalamus and caudate) were found significant (p<0.01) with small effect sizes (<0.15). A detailed overview of this statistical evaluation can be found in Fig. S2.

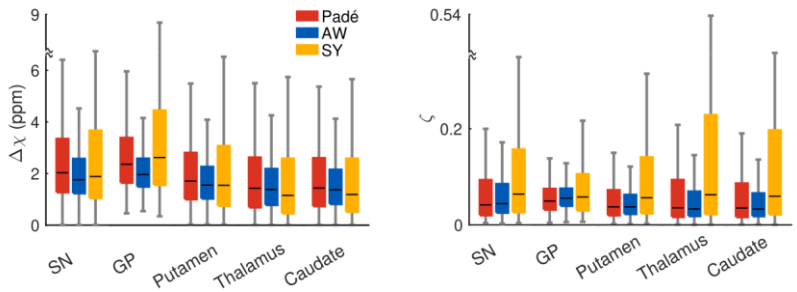

Fig. 6. Properties of the magnetic inclusions present within brain tissue, estimated from the values of $R^*_{2,micro}$ and $\langle\Omega^2\rangle$ under the assumption of the SDR. The magnetic susceptibility of the inclusions is larger in the SN and GP (median $\Delta\chi$~2 ppm) compared to the remaining regions ($\Delta\chi$~1.4 ppm). The GP exhibits the largest volume fraction of inclusions (median ζ~0.06).

Under the assumption of the DNR (Fig. 7), the estimates of $R^*_{2,micro}$ and $\langle\Omega^2\rangle$ were used to compute the value of the parameters τ and α (Eqs. 7 and 8b). The estimates of τ are larger in the putamen, thalamus, and caudate (median ~1.6 ms) than in the SN and GP (median ~1.1 ms). A typical value of τ~1.5 ms suggests that the magnetic field inhomogeneities generated by the inclusions have a typical radius r~3 μm, in the order of a typical cell size. The value of α is similar across regions (median ~0.10-0.16), consistent with the assumption of the DNR ($\alpha \ll 1$).

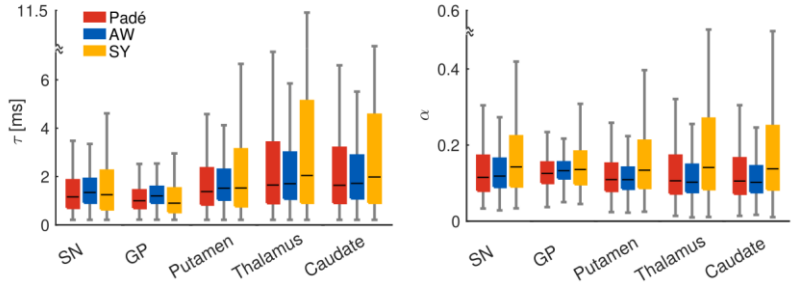

Fig. 7. Properties of the magnetic inclusions present within brain tissue, estimated from the values of $R^*_{2,micro}$ and $\langle\Omega^2\rangle$ under the assumption of the DNR. The characteristic diffusion times τ are larger in the putamen, thalamus, and caudate (median ~1.6 ms) compared to SN and GP (~1.1 ms). The corresponding estimates of the radius of the magnetic field inhomogeneities generated by the inclusions (r ~3 μm) are in the order of a typical cell size. α values are similar across regions (median ~0.10-0.16) and consistent with the assumption of the DNR.

Under the assumption of the SDR, estimates of the MRI magnetic susceptibility (χ_{MRI}) were computed from the estimates of ζ and $\Delta\chi$ (Eq. 9). With the AW and Padé approximations, the χ_{MRI} estimates are ~0.11 ppm in the GP, ~0.08 ppm in the SN, ~0.06 ppm in the putamen, and ~0.05 ppm in the thalamus and caudate (Fig. 8). The estimates of χ_{MRI} from the SY model are systematically higher by ~0.03 ppm. These values are consistent with susceptibility

estimates obtained from QSM techniques (Bilgic et al., 2012; Langkammer et al., 2012; Yablonskiy et al., 2021).

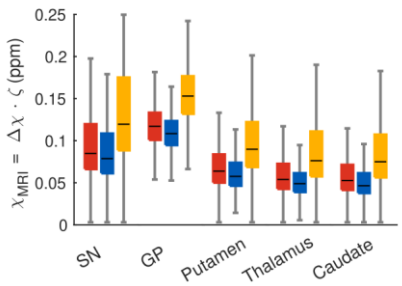

Fig. 8. MRI magnetic susceptibility ($\chi_{MRI} = \Delta\chi \cdot \zeta$) computed under the assumption of the SDR. The values of χ_{MRI} are consistent with estimates obtained using QSM techniques (Bilgic et al., 2012; Langkammer et al., 2012; Yablonskiy et al., 2021).

5 Discussion

Here we provide experimental evidence of non-exponential signal decay due to transverse relaxation in *in vivo* MRI data from subcortical regions. In agreement with theoretical studies, signal decay follows a Gaussian behaviour at short echo times with a transition to exponential behaviour at long echo times. Models of the effect on the MRI signal of magnetic inclusions within brain tissue show an improved fit to the data compared to the widely used exponential model. The strongest deviations from exponential behaviour were found in iron-rich areas, such as the GP and SN. From the estimates of the model parameters, we estimated the properties of the magnetic inclusions at the source of the effect. The results are consistent with histological studies of iron distribution within brain tissue and suggest that non-exponential signal decay arises from spatially localized iron-rich cells.

5.1 Non-exponential transverse relaxation decay

The lack of evidence of non-exponential signal decay in subcortical regions has been attributed to the short timescale of the transition between the Gaussian and exponential behaviours, below the range of achievable echo times (Yablonskiy et al., 2021). Here, we combined a dense sampling of the decay curve with acquisition strategies that reduce the noise level in the data (Castella et al., 2018; Raynaud et al., 2023) to collect reliable evidence of non-exponential signal decay. Transverse relaxation decay exhibits a Gaussian behaviour at short echo times ($T_E \lesssim 5$ms) with a transition towards exponential decay (Fig. 1). This behaviour was predominantly observed in subcortical grey matter regions (Fig. 3) and is consistent with theoretical models of the effect on the MRI signal of magnetic inclusions within brain tissue (Kiselev and Novikov, 2002; Novikov and Kiselev, 2008). These models show improved fit to the data compared with the widely used exponential model (Fig. 2). Amongst subcortical regions, the strongest non-exponential behaviours take place in the GP and SN.

The higher values of $R^*_{2,micro}$ and $\langle\Omega^2\rangle$ in the SN and GP (Fig. 4) are consistent with the higher concentration of iron in these regions (Hallgren and Sourander, 1958; Haacke et al., 2005; Langkammer et al., 2012; Krebs et al., 2014) and with the expected dependence of these parameters on iron concentration (Eqs. 7 and 8). However, other magnetic materials such as myelin or blood vessels might also contribute, particularly in the thalamus due to its comparatively high myelin and low iron concentrations (Hallgren and Sourander, 1958).

We considered a model-free Padé approximation and two models of the MRI signal generated by brain tissue with magnetic inclusions. All corresponding expressions fitted the data equally well, with marginal differences between them (Fig. 2). Nonetheless, the SY model yields higher estimates of $R^*_{2,micro}$ and $\langle\Omega^2\rangle$ compared to the AW model and Padé approximations. This results from the long transition from the Gaussian to exponential behaviours predicted by the SY model, due to the square-root term in Eq. 5. As a result, the exponential decay rate predicted by the SY model differs from the one observable experimentally (Fig. 5).

5.2 Characterization of magnetic inclusions within subcortical tissue

From the estimates of the signal model parameters, we were able to estimate the properties of the magnetic inclusions embedded within brain tissue. This would not have been achievable from the exponential end of the decay alone. This was conducted under the assumption of the SDR (Fig. 6) and DNR (Fig. 7) for which different analytical expressions exist.

The estimates of the magnetic susceptibility of the inclusions, obtained under the assumption of the SDR, lie in the range $\Delta\chi$~1-2 ppm across subcortical regions and MRI signal models. The ordering of the $\Delta\chi$ estimates between subcortical values follows the ordering of *ex vivo* measures of iron concentration within brain tissue (Hallgren and Sourander, 1958; Haacke et al., 2005; Langkammer et al., 2012; Krebs et al., 2014). The estimates of $\Delta\chi$ are in good agreement with the magnetic susceptibility of iron-rich neuromelanin aggregates in the SN (Brammerloh et al., 2021). Under the assumption that ferritin is the only magnetic material within the tissue, these susceptibility estimates lead to estimates of iron concentration $[Fe]$~1-2 mg/g within the inclusions, well in-line with the intra-cellular concentrations of iron known from *ex vivo* studies (Friedrich et al., 2021). The estimates of the volume fraction of the inclusions lie in the range $\zeta\sim$ 0.03-0.06 across subcortical regions and MRI signal models. The ordering of the ζ estimates between subcortical values also follows the ordering of *ex vivo* measures of iron concentration within brain tissue (Hallgren and Sourander, 1958; Haacke et al., 2005; Langkammer et al., 2012; Krebs et al., 2014). The estimates of ζ are in broad agreement with those calculated considering the distribution of iron at the cellular scale: $\zeta_{cell} = \frac{[Fe]_{bulk}}{[Fe]_{cell}}$~0.01, with $[Fe]_{bulk}$~0.02 mg/g (Hallgren and Sourander, 1958) and $[Fe]_{cell}$~1.5 mg/g (Friedrich et al., 2021). In addition, our ζ estimates are in line with the experimental volume fractions of neuromelanin observed in the SN (Brammerloh et al., 2021). Overall, these results indicate that the reported non-exponential signal decay arises from spatially localized clusters consistent with iron-loaded cells.

The consistency of the estimates of the properties of the magnetic inclusions with *ex vivo* studies highlights the plausibility of the SDR as the regime underlying transverse relaxation decay in subcortical grey matter. The estimates of MRI magnetic susceptibility, computed from the properties of the inclusions under the assumption of the SDR ($\chi_{MRI} = \zeta\Delta\chi$, Fig. 8), are also consistent with those obtained from QSM techniques (~0.1 ppm, (Bilgic et al., 2012; Langkammer et al., 2012; Yablonskiy et al., 2021)).

Under the assumption of the DNR, the values of the signal decay parameters were used to estimate the parameter τ, the decay time of the frequency auto-correlation of water molecules diffusing through the inhomogeneous magnetic field generated by the inclusions. The τ estimates (~1.5 ms) suggest a typical radius of ~3 μm for the magnetic inclusions. In agreement with the SDR analysis, this finding suggests that cell-sized iron clusters are at the source of the non-exponential decay. This estimate of r is also consistent with the cell-based definition of the radius of magnetic inclusions proposed by Taege et al., 2019 and with the

value of r reported in studies of excised human grey matter tissue (Jensen and Chandra, 2000a). In particular, the latter study also reported larger values of r in the putamen, thalamus, and caudate, compared to the GP as observed here (Fig. 7). The estimated radius of ~3 μm exceeds the size threshold for iron aggregates that would make the DNR plausible (Yablonskiy et al., 2021). Under the DNR, the parameters $\Delta\chi$ and ζ could not be estimated. Instead, we estimated the parameter $\alpha = \tau\sqrt{\langle\Omega^2\rangle}$. The resulting estimates are smaller than 1, suggesting that the time scale τ at which molecules diffuse is smaller than the time scale of spin dephasing caused by magnetic material, consistently with the assumptions of the DNR theory. However, the parameter α was computed from estimates of the mean square frequency deviations averaged across a voxel $\langle\Omega^2\rangle$, rather than from the mean frequency generated by a single magnetic inclusion Ω_s, as defined by theoretical studies ($\langle\Omega^2\rangle \propto \zeta\, \langle{\Omega_s}^2\rangle$) (Yablonskiy and Haacke, 1994; Kiselev and Novikov, 2002).

The SDR has been proposed as a valid explanation for iron-induced transverse relaxation in subcortical grey matter, due to the large differences between the relaxation rates in gradient-echo and spin-echo data (Sedlacik et al., 2014; Brammerloh et al., 2021). However, studies of the relationship between R_2^* and magnetic susceptibility suggest that the contribution of iron to relaxation in the basal ganglia can be described under the DNR, provided that iron is aggregated in clusters with ~100 nm radius (Shin et al., 2021; Yablonskiy et al., 2021). The most plausible scenario is that transverse relaxation is the result of a combination of both regimes. Therefore, approaches that allow to interpolate between these two limiting cases may allow a more accurate characterization of the magnetic inclusions at the source of non-exponential transverse relaxation in subcortical brain regions (Bauer and Nadler, 2002; Ziener et al., 2005).

6 Conclusions

In this study, we provided experimental evidence of non-exponential transverse relaxation from *in vivo* gradient-echo MRI data in subcortical brain regions at 3T. The behaviour of the decay is consistent with the effect of magnetic inclusions on the MRI signal predicted by theoretical studies. These theoretical models of the MRI signal yield improved fit with experimental data compared to the widely used exponential model. The larger deviations from exponential decay were observed in iron-rich subcortical regions (substantia nigra, globus pallidus). From the estimates of the signal decay parameters, we characterized the distribution of the magnetic inclusions within brain tissue at the source of the non-exponential decay. Our estimates are consistent with *ex vivo* studies of iron distribution within brain tissue and suggest that the observed non-exponential signal decay arises from spatially localized iron-rich cells.

Non-exponential decay of the MRI signal due to transverse relaxation allows the characterization of iron-rich inclusions within subcortical structures from *in vivo* MRI data and provides new opportunities for the study of iron-related brain changes in neurodegenerative diseases.

7 Conflict of Interest

The authors declare no conflict of interest.

8 Author Contributions

RO: Conceptualization, Methodology, Investigation, Formal analysis, Writing-Original draft, Writing – Review and Editing, QR: Investigation, Writing – Review and Editing, VK: Conceptualization, Writing – Review & Editing, IJ: Conceptualization, Writing – Review & Editing, AL: Conceptualization, Methodology, Investigation, Formal analysis, Writing-Original draft, Writing – Review and Editing, Supervision, Project administration, Funding acquisition.

9 Funding

AL is supported by the Swiss National Science Foundation (grant no 320030 184784) and the ROGER DE SPOELBERCH Foundation. IJ is supported by the Swiss National Science Foundation (grant no PCEFP2_194260).

10 Data and code availability

The code and data used for this analysis will be made publicly available upon publication.

11 References

Anderson, P. W., and Weiss, P. R. (1953). Exchange Narrowing in Paramagnetic Resonance. *Exch. Organ. Behav. Teach. J.* 679.

Ashburner, J., and Friston, K. J. (2005). Unified segmentation. *Neuroimage* 26, 839–851. doi: 10.1016/j.neuroimage.2005.02.018.

Barber, T. W., Brockway, J. A., and Higgins, L. S. (1970). THE DENSITY OF TISSUES IN AND ABOUT THE HEAD. *Acta Neurol. Scandinav.* 46, 85-92,.

Bauer, W. R., and Nadler, W. (2002). Spin dephasing in the extended strong collision approximation. *Phys. Rev. E - Stat. Physics, Plasmas, Fluids, Relat. Interdiscip. Top.* 65, 1–15. doi: 10.1103/PhysRevE.65.066123.

Bilgic, B., Pfefferbaum, A., Rohlfing, T., Sullivan, E. V., and Adalsteinsson, E. (2012). MRI estimates of brain iron concentration in normal aging using quantitative susceptibility mapping. *Neuroimage* 59, 2625–2635. doi: 10.1016/j.neuroimage.2011.08.077.

Brammerloh, M., Morawski, M., Friedrich, I., Reinert, T., Lange, C., Pelicon, P., et al. (2021). Measuring the iron content of dopaminergic neurons in substantia nigra with MRI relaxometry. *Neuroimage* 239. doi: 10.1016/j.neuroimage.2021.118255.

Castella, R., Arn, L., Dupuis, E., Callaghan, M. F., Draganski, B., and Lutti, A. (2018). Controlling motion artefact levels in MR images by suspending data acquisition during periods of head motion. *Magn. Reson. Med.* 80, 2415–2426. doi: 10.1002/mrm.27214.

Corbin, N., Oliveira, R., Raynaud, Q., Di Domenicantonio, G., Draganski, B., Kherif, F., et al. (2023). Statistical analyses of motion-corrupted MRI relaxometry data computed from multiple scans. *J. Neurosci. Methods* 398. doi: 10.1016/j.jneumeth.2023.109950.

Damulina, A., Pirpamer, L., Soellradl, M., Sackl, M., Tinauer, C., Hofer, E., et al. (2020). Cross-sectional and longitudinal assessment of brain iron level in Alzheimer disease using 3-T MRI. *Radiology* 296, 619–626. doi: 10.1148/radiol.2020192541.

Deistung, A., Schweser, F., and Reichenbach, J. R. (2017). Overview of quantitative susceptibility mapping. *NMR Biomed.* 30. doi: 10.1002/nbm.3569.

Does, M. D., Olesen, J. L., Harkins, K. D., Serradas-Duarte, T., Gochberg, D. F., Jespersen, S. N., et al. (2019). Evaluation of principal component analysis image denoising on multi-exponential MRI relaxometry. *Magn. Reson. Med.* 81, 3503–3514. Available at: https://onlinelibrary.wiley.com/doi/full/10.1002/mrm.27658.

Friedrich, I., Reimann, K., Jankuhn, S., Kirilina, E., Stieler, J., Sonntag, M., et al. (2021). Cell specific quantitative iron mapping on brain slices by immuno-μPIXE in healthy elderly and Parkinson's disease. *Acta Neuropathol. Commun.* 9, 1–17. doi: 10.1186/s40478-021-01145-2.

Fukunaga, M., Li, T. Q., Van Gelderen, P., De Zwart, J. A., Shmueli, K., Yao, B., et al. (2010). Layer-specific variation of iron content in cerebral cortex as a source of MRI contrast. *Proc. Natl. Acad. Sci. U. S. A.* 107, 3834–3839. doi: 10.1073/pnas.0911177107.

Gerlach, M., Ben-Shachar, D., Riederer, P., and Youdim, M. B. H. (1994). Altered brain metabolism of iron as a cause of neurodegenerative diseases? *J. Neurochem.* 63, 793–807. doi: 10.1046/j.1471-4159.1994.63030793.x.

Haacke, E. M., Cheng, N. Y. C., House, M. J., Liu, Q., Neelavalli, J., Ogg, R. J., et al. (2005). Imaging iron stores in the brain using magnetic resonance imaging. *Magn. Reson. Imaging* 23, 1–25. doi: 10.1016/j.mri.2004.10.001.

Hallgren, B., and Sourander, P. (1958). The effect of age on non-haemin iron in the human brain. *J. Neurochem.* 3, 41–51. doi: 10.1136/jnnp.50.2.231.

Hare, D., Ayton, S., Bush, A., and Lei, P. (2013). A delicate balance: Iron metabolism and diseases of the brain. *Front. Aging Neurosci.* 5, 1–19. doi: 10.3389/fnagi.2013.00034.

Helms, G., Dathe, H., and Dechent, P. (2008a). Quantitative FLASH MRI at 3T using a rational approximation of the Ernst

equation. *Magn. Reson. Med.* 59, 667–672. doi: 10.1002/mrm.21542.
Helms, G., Dathe, H., Kallenberg, K., and Dechent, P. (2008b). High-resolution maps of magnetization transfer with inherent correction for RF inhomogeneity and T1 relaxation obtained from 3D FLASH MRI. *Magn. Reson. Med.* 60, 1396–1407. doi: 10.1002/mrm.21732.
Jensen, J. H., and Chandra, R. (1999). Transverse relaxation time field dependence for tissues with microscopic magnetic susceptibility variations. *Proc. Int. Soc. Mag. Reson. Med.* 7, 656.
Jensen, J. H., and Chandra, R. (2000a). NMR relaxation in tissues with weak magnetic inhomogeneities. *Magn. Reson. Med.* 44, 144–156. doi: 10.1002/1522-2594(200007)44:1<144::AID-MRM21>3.0.CO;2-O.
Jensen, J. H., and Chandra, R. (2000b). Strong field behavior of the NMR signal from magnetically heterogeneous tissues. *Magn. Reson. Med.* 43, 226–236. doi: 10.1002/(SICI)1522-2594(200002)43:2<226::AID-MRM9>3.0.CO;2-P.
Kennan, R. P., Zhong, J., and Gore, J. C. (1994). Intravascular susceptibility contrast mechanisms in tissues. *Magn. Reson. Med.* 31, 9–21. doi: 10.1002/mrm.1910310103.
Kiselev, V. G., and Novikov, D. S. (2002). Transverse NMR Relaxation as a Probe of Mesoscopic Structure. *Phys. Rev. Lett.* 89, 2–5. doi: 10.1103/PhysRevLett.89.278101.
Kiselev, V. G., and Novikov, D. S. (2018). Transverse NMR relaxation in biological tissues. *Neuroimage* 182, 149–168. doi: 10.1016/j.neuroimage.2018.06.002.
Krebs, N., Langkammer, C., Goessler, W., Ropele, S., Fazekas, F., Yen, K., et al. (2014). Assessment of trace elements in human brain using inductively coupled plasma mass spectrometry. *J. Trace Elem. Med. Biol.* 28, 1–7. doi: 10.1016/j.jtemb.2013.09.006.
Langkammer, C., Krebs, N., Goessler, W., Scheurer, E., Ebner, F., Yen, K., et al. (2010). Quantitative MR imaging of brain iron: A postmortem validation study. *Radiology* 257, 455–462. doi: 10.1148/radiol.10100495.
Langkammer, C., Schweser, F., Krebs, N., Deistung, A., Goessler, W., Scheurer, E., et al. (2012). Quantitative susceptibility mapping (QSM) as a means to measure brain iron? A post mortem validation study. *Neuroimage* 62, 1593–1599. doi: 10.1016/j.neuroimage.2012.05.049.
Li, L., and Leigh, J. S. (2004). Quantifying Arbitrary Magnetic Susceptibility Distributions with MR. *Magn. Reson. Med.* 51, 1077–1082. doi: 10.1002/mrm.20054.
Lutti, A., Corbin, N., Ashburner, J., Ziegler, G., Draganski, B., Phillips, C., et al. (2022). Restoring statistical validity in group analyses of motion- corrupted MRI data. *Hum. Brain Mapp.*, 1–11. Available at: 10.1002/hbm.25767.
Lutti, A., Hutton, C., Finsterbusch, J., Helms, G., and Weiskopf, N. (2010). Optimization and validation of methods for mapping of the radiofrequency transmit field at 3T. *Magn. Reson. Med.* 64, 229–238. doi: 10.1002/mrm.22421.
Lutti, A., Stadler, J., Josephs, O., Windischberger, C., Speck, O., Bernarding, J., et al. (2012). Robust and fast whole brain mapping of the RF transmit field B1 at 7T. *PLoS One* 7, 1–7. doi: 10.1371/journal.pone.0032379.
Maclaren, J., Armstrong, B. S. R., Barrows, R. T., Danishad, K. A., Ernst, T., Foster, C. L., et al. (2012). Measurement and Correction of Microscopic Head Motion during Magnetic Resonance Imaging of the Brain. *PLoS One* 7, 3–11. doi: 10.1371/journal.pone.0048088.
Möller, H. E., Bossoni, L., Connor, J. R., Crichton, R. R., Does, M. D., Ward, R. J., et al. (2019). Iron , Myelin , and the Brain : Neuroimaging Meets Neurobiology. *Trends Neurosci.* 42, 384–401. doi: 10.1016/j.tins.2019.03.009.
Novikov, D. S., and Kiselev, V. G. (2008). Transverse NMR relaxation in magnetically heterogeneous media. *J. Magn. Reson.* 195, 33–39. doi: 10.1016/j.jmr.2008.08.005.
Novikov, D. S., Kiselev, V. G., and Jespersen, S. N. (2018). On modeling. *Magn. Reson. Med.* 79, 3172–3193. doi: 10.1002/mrm.27101.
Péran, P., Cherubini, A., Luccichenti, G., Hagberg, G., Démonet, J. F., Rascol, O., et al. (2009). Volume and iron content in basal ganglia and thalamus. *Hum. Brain Mapp.* 30, 2667–2675. doi: 10.1002/hbm.20698.
Raynaud, Q., Domenicantonio, G. Di, Yerly, J., Dardano, T., Heeswijk, R. B. van, and Lutt, A. (2023). A characterization of cardiac-induced noise in R2* maps of the brain. *Magn. Reson. Med.*, 1–15. doi: 10.2307/2318215.
Schenck, J. F. (1992). Health and Physiological Effects of Human Exposure to Whole-Body Four-Tesla Magnetic Fields during MRI. *Ann. N. Y. Acad. Sci.* 649, 285–301. doi: 10.1111/j.1749-6632.1992.tb49617.x.
Schweser, F., Deistung, A., Lehr, B. W., and Reichenbach, J. R. (2011). Quantitative imaging of intrinsic magnetic tissue properties using MRI signal phase: An approach to in vivo brain iron metabolism? *Neuroimage* 54, 2789–2807. doi: 10.1016/j.neuroimage.2010.10.070.
Sedlacik, J., Boelmans, K., Löbel, U., Holst, B., Siemonsen, S., and Fiehler, J. (2014). Reversible, irreversible and effective transverse relaxation rates in normal aging brain at 3T. *Neuroimage* 84, 1032–1041. doi: 10.1016/j.neuroimage.2013.08.051.
Shin, H. G., Lee, J., Yun, Y. H., Yoo, S. H., Jang, J., Oh, S. H., et al. (2021). χ-separation: Magnetic susceptibility source separation toward iron and myelin mapping in the brain. *Neuroimage* 240, 118371. doi: 10.1016/j.neuroimage.2021.118371.
Storey, P., Chung, S., Ben-Eliezer, N., Lemberskiy, G., Lui, Y. W., and Novikov, D. S. (2015). Signatures of Microstructure in Conventional Gradient and Spin Echo Signals. in *Proc. 23rd Annual Meeting ISMRM, Toronto, Canada*, 014.
Sukstanskii, A. L., and Yablonskiy, D. A. (2003). Gaussian approximation in the theory of MR signal formation in the presence of structure-specific magnetic field inhomogeneities. *J. Magn. Reson.* 163, 236–247. doi: 10.1016/S1090-7807(03)00131-9.
Tabelow, K., Balteau, E., Ashburner, J., Callaghan, M. F., Draganski, B., Helms, G., et al. (2019). hMRI – A toolbox for quantitative MRI in neuroscience and clinical research. *Neuroimage* 194, 191–210. doi: 10.1016/j.neuroimage.2019.01.029.
Taege, Y., Hagemeier, J., Bergsland, N., Dwyer, M. G., Weinstock-Guttman, B., Zivadinov, R., et al. (2019). Assessment of mesoscopic properties of deep gray matter iron through a model-based simultaneous analysis of magnetic

susceptibility and R2* - A pilot study in patients with multiple sclerosis and normal controls. *Neuroimage* 186, 308–320. doi: 10.1016/j.neuroimage.2018.11.011.
Thompson, K. J., Shoham, S., and Connor, J. R. (2001). Iron and neurodegenerative disorders. *Brain Res. Bull.* 55, 155–164. doi: 10.1016/S0361-9230(01)00510-X.
Ulla, M., Bonny, J. M., Ouchchane, L., Rieu, I., Claise, B., and Durif, F. (2013). Is R2* a New MRI Biomarker for the Progression of Parkinson's Disease? A Longitudinal Follow-Up. *PLoS One* 8, 1–8. doi: 10.1371/journal.pone.0057904.
Ulrich, X., and Yablonskiy, D. A. (2016). Separation of cellular and BOLD contributions to T2∗ signal relaxation. *Magn. Reson. Med.* 75, 606–615. doi: 10.1002/mrm.25610.
Ward, R. J., Zucca, F. A., Duyn, J. H., Crichton, R. R., and Zecca, L. (2014). The role of iron in brain ageing and neurodegenerative disorders. *Lancet Neurol.* 13, 1045–1060. doi: 10.1016/S1474-4422(14)70117-6.
Weiskopf, N., Callaghan, M. F., Josephs, O., Lutti, A., and Mohammadi, S. (2014). Estimating the apparent transverse relaxation time (R2*) from images with different contrasts (ESTATICS) reduces motion artifacts. *Front. Neurosci.* 8, 1–10. doi: 10.3389/fnins.2014.00278.
Yablonskiy, D. A., and Haacke, E. M. (1994). Theory of NMR signal behavior in magnetically inhomogeneous tissues: The static dephasing regime. *Magn. Reson. Med.* 32, 749–763. doi: 10.1002/mrm.1910320610.
Yablonskiy, D. A., Wen, J., Kothapalli, S. V. V. N., and Sukstanskii, A. L. (2021). In vivo evaluation of heme and non-heme iron content and neuronal density in human basal ganglia. *Neuroimage* 235, 118012. doi: 10.1016/j.neuroimage.2021.118012.
Yao, B., Li, T. Q., Gelderen, P. van, Shmueli, K., de Zwart, J. A., and Duyn, J. H. (2009). Susceptibility contrast in high field MRI of human brain as a function of tissue iron content. *Neuroimage* 44, 1259–1266. doi: 10.1016/j.neuroimage.2008.10.029.
Zaitsev, M., Dold, C., Sakas, G., Hennig, J., and Speck, O. (2006). Magnetic resonance imaging of freely moving objects: prospective real-time motion correction using an external optical motion tracking system. *Neuroimage* 31, 1038–1050. doi: 10.1016/j.neuroimage.2006.01.039.
Ziener, C. H., Bauer, W. R., and Jakob, P. M. (2005). Transverse relaxation of cells labeled with magnetic nanoparticles. *Magn. Reson. Med.* 54, 702–706. doi: 10.1002/mrm.20634.

Supplementary

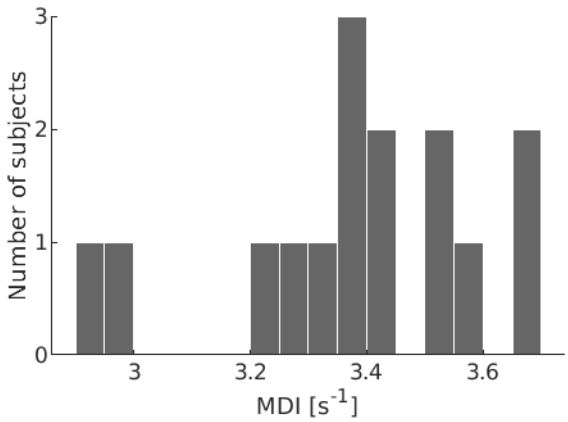

Figure S1. Distribution of Motion Degradation Index (MDI) across subjects and repetitions.

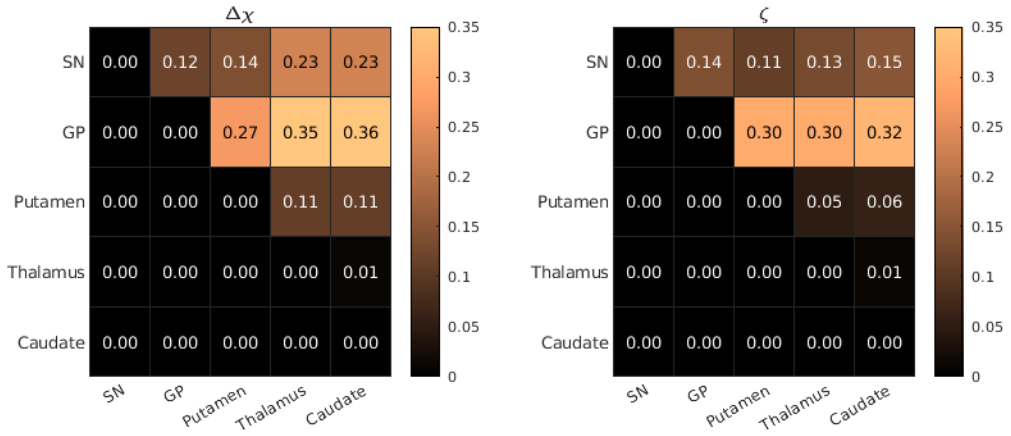

Figure S2. Absolute effect size (cliff's delta) of the differences in $\Delta\chi$ and ζ between subcortical regions for the AW models. A value of 0 suggests no difference between the two regions, while values closer to 1 indicate stronger associations. The p-values are not shown given that excluding the pair thalamus and caudate, all the remaining pairwise comparisons were significant (due to the large sample size). Note that given that the matrix is symmetric only the upper part is shown.